

Altermagnetic phase transition in a Lieb metal

Matteo Dürrnagel,^{*} Hendrik Hohmann,^{*} Atanu Maity, Jannis Seufert, Michael Klett, Lennart Klebl, and Ronny Thomale[†]

*Institut für Theoretische Physik und Astrophysik and Würzburg-Dresden Cluster of Excellence ct.qmat,
Universität Würzburg, 97074 Würzburg, Germany*

(Dated: December 20, 2024)

We analyze the phase transition between a symmetric metallic parent state and itinerant altermagnetic order. The underlying mechanism we reveal in our microscopic model of electrons on a Lieb lattice does not involve orbital ordering, but derives from sublattice interference.

Introduction—Triggered by the discovery of high- T_c superconductivity in copper oxides, the possibility of unconventional pairing transcended our perspective on Fermi surface instabilities. Even though the individual two-electron ground state would always favor zero relative angular momentum according to the Perron-Frobenius theorem [1, 2], the condensation energy gain to the quantum fluid formed by phase-coherent Cooper pairs drives the preference of a d -wave particle-particle condensate, i.e., a pairing state with finite relative angular momentum. While the field has been aware of its principal possibility for decades, it has proven challenging to microscopically identify a similarly unconventional magnet, i.e., a spinful particle-hole condensate with finite relative angular momentum [3]. In combination with translation symmetry breaking, a rare instance is the kagome Hubbard model exhibiting a p -wave spin bond order [4]. In combination with point group symmetry breaking, a spin-type d -wave nematic order has been claimed in the context of higher order van-Hove singularities [5], but has not yet unfolded in a generic microscopic model. The omnipresent difficulty in realizing such states is engraved in the oppositely charged constituents of the particle-hole pairs forming the quantum fluid, as they are naturally expected to gain condensation energy from zero relative angular momentum between particle and hole [6, 7].

A new chapter on broadening the phenomenological scope of exotic magnetic order has started with the discovery of a seemingly unprecedented type of magnetic order in 2019, now termed altermagnetism (AM) [8–13]. The key driving interest rests upon the potential use of AMs for spintronics, as their energetically spin-split magnetic excitations, along with zero net magnetization, advantageously combine antiferromagnetic and ferromagnetic features for technological utilization [14–17]. A collinear AM is designed such that sites with opposite-spin orientation transform into each other by spatial rotation [18, 19]. While this conceptually resembles the intertwining of time reversal and point group symmetry related to spin Pomeranchuk instabilities, a core insight embodied by the rising AM research domain

is that such intertwining can just as well be more trivially achieved in a scale-separated cascade of transitions: As of now, the aspired abundance of AMs builds on the formation of anisotropies at the crystal field energy scale, followed by an independent magnetic transition determined by local moments and additional low-energy electronic scales [20, 21]. A complete magnetic analogue of unconventional superconducting pairing, however, would only be resembled by the microscopic realization of a metallic parent state subject to a single phase transition into AM order [22, 23].

In this Letter, we formulate a microscopic realization of an altermagnetic phase transition for interacting electrons on the Lieb lattice. Previous attempts to overcome the scale-separated nature of AM formation revolved around interacting electrons subject to combined staggered orbital and antiferromagnetic ordering. These proposals, however, are contrived in some aspects, as the natural propensity of a staggered orbitally ordered system to form a ferromagnet due to Hund’s coupling can only be avoided by ignoring the Hund’s coupling altogether [24, 25]. Instead, we seek to intertwine rotation and time-reversal symmetry through the sublattice interference (SI) profile found in a single-orbital Lieb metal parent state [26]. Originally introduced for the kagome lattice [4, 27, 28], SI ascribes pivotal relevance to the sublattice distribution of Fermi level eigenstates with regard to identifying the relevant scattering channels for the unfolding electronic order. On the Lieb lattice, such interference leads to a dissociation of sublattice contributions to the magnetic fluctuation profile of the Lieb metal parent state. Through functional renormalization group (FRG) calculations [29–32], we show how this yields a phase transition into an AM phase. We classify the emerging order to descend from a d -wave spin Pomeranchuk instability, and to reveal a spin-split quasiparticle bandstructure featuring symmetry-protected nodal lines.

Model—We start from tightly bound electrons on a Lieb lattice, which is a square-depleted 2D lattice with three sites per unit cell and features equivalent nearest neighbor bonds connecting inequivalent sites. While it is rarely the lattice structure that minimizes a generic crystal field potential, the Lieb lattice forms a central building block of (layered) perovskites [33], and as such is relevant for high- T_c copper oxides when the oxygen

^{*} These authors contributed equally.

[†] ronny.thomale@uni-wuerzburg.de

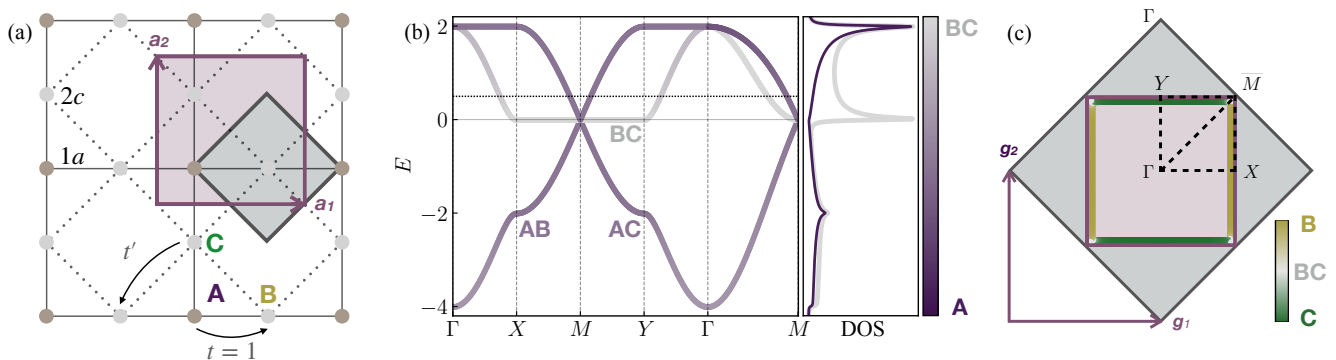


FIG. 1. (a) Real space lattice structure with of the Lieb lattice. The purple square marks the unit cell with the A site on the trivial Wyckoff position ($1a$), and the B and C sites on the $2c$ Wyckoff positions. Nearest- and next-nearest neighbor hoppings t and t' are indicated. The gray square corresponds to the unit cell of a lattice without the A site, i.e., a simple square lattice. (b) Resulting band structure along the high-symmetry path indicated in panel (c) for $t' = t/2$ and $\mu_A = 0$. We overlay the sublattice content by color (purple: A , gray: B/C). The right panel displays the sublattice resolved density of states, with the B/C polarized van-Hove singularity at the band touching point. (c) Brillouin zones (BZ) of the Lieb lattice structure (purple) and the intercalated square lattice (gray) formed by dashed lines connecting the $2c$ Wyckoff positions. We additionally plot the Fermi surface and its sublattice polarization (yellow: B , green: C), which is pure along the BZ boundaries and mixed at the van-Hove points M .

sites are not integrated out, but kept for their low-energy description [34]. Figure 1a illustrates the sublattices on Wyckoff positions $1a$ (A) and $2c$ (B, C). While the A site transforms trivially under all elements of C_{4v} , the sites B and C map onto each other under C_4 rotations. This transformation behavior is inherited by the tight-binding Hamiltonian. It reads

$$H = - \sum_{ij,\sigma} t_{ij} c_{i\sigma}^\dagger c_{j\sigma} - \sum_{i,\sigma} \mu_i n_{i\sigma} + U \sum_i n_{i\uparrow} n_{i\downarrow}, \quad (1)$$

where the operator $c_{i\sigma}^{(\dagger)}$ annihilates (creates) an electron with spin σ on site i , $n_{i\sigma} = c_{i\sigma}^\dagger c_{i\sigma}$ is the density operator, μ_i denotes the chemical potential at site i , and U is the Hubbard onsite repulsion. We employ an extended Lieb lattice model by setting $t_{ij} = 1$ for nearest neighbors (NN, A - B and A - C bonds, solid lines in Fig. 1a) and $t_{ij} = t'$ for next-nearest neighbors (NNN, B - C bonds, dashed lines). To allow for the effect of different atomic species at Wyckoff positions $1a$ (A) and $2c$ (B, C), we include an intrinsic detuning $\mu_A \neq \mu_{B,C}$.

While the electronic spectrum of the metallic parent state displays the full space group symmetry, the multi-site unit cell exhibits a non-trivial transformation behaviour of the eigenstates (Bloch functions). For the Lieb lattice with NN hopping only ($t' = 0$), a flat band resides at the Fermi level featuring a distinct sublattice polarization on the zone boundary: Excluding the zone corner at M , only the B and C sites contribute to the electronic eigenstates (see SM [35] for details) [26]. While this feature persists in the presence of NNN hopping t' , the flat band attains a sizable dispersion away from the zone boundary, producing a van-Hove singularity (VHS, see Fig. 1b). At the van-Hove M point, the system displays a topologically protected quadratic (triple) band

touching for $\mu_A \neq 0$ ($\mu_A = 0$) [33]. Even at pristine filling (dashed line in Fig. 1b), the proximate VHS implies a large density of states (DOS) participating in a tentative Fermi surface instability, rendering the system already unstable against weak repulsive interactions. The single-particle spectrum and sublattice polarization can be understood by decomposing the extended Lieb lattice into two intercalated square lattices. The B and C sublattice form a regular square lattice with lattice constant $1/\sqrt{2}$ and NN hopping t' , which is coupled to the larger square lattice of the site A via t (cf. Fig. 1a). Comparing the Brillouin zone (BZ) of the associated unit cells in Fig. 1c, the Fermi surface (FS) at the zone boundary reveals itself as the characteristic FS of the smaller square lattice (gray) backfolded to the Lieb lattice BZ (purple). While the weight of the B and C sublattices must be equal and constant in the $t = 0$ limit, the Lieb lattice structure allows for SI along the FS, manifesting in B/C polarization along different directions. Regardless of the value of t' , we find that the eigenstate along X - M (Y - M) displays full C (B) polarization. In turn, the high-energy VHSs display a strong AB/AC mixing (see Fig. 1b). This behavior is reminiscent of the pure/mixed VHSs found in the kagome lattice [28, 36–38].

AM order—Our Lieb metallic parent state implies an itinerant setup in which we investigate the unfolding of AM order. By contrast, as inspired by their *ab initio* theoretical description, the prevalent perspective on AMs is the formation of local magnetic moments at high energy, and the subsequent low-energy magnetic ordering derives from antiferromagnetic exchange couplings of local moments in the given lattice geometry. This is why the symmetry classification of AMs deriving from local moments does not necessarily include all possible symmetry specifications of itinerant AMs [39]. Starting from

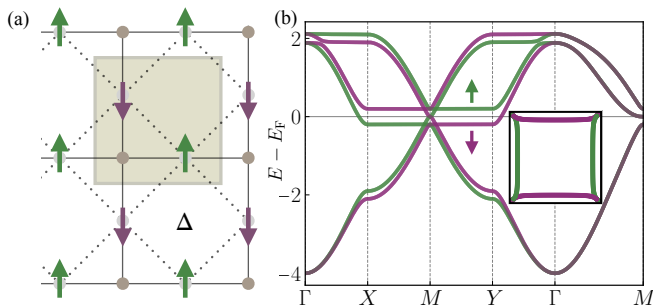


FIG. 2. d -wave altermagnetic state on the Lieb lattice. (a) Real space magnetization pattern in the B_1 irreducible representation of C_{4v} . The magnetic order parameter Δ is nonzero only on the B and C sites. (b) Quasiparticle band structure in the altermagnetic phase for $t' = t/2$, $\mu_A = 0$, and $\Delta_M = 0.2t$ with spin polarization indicated by purple/green (\downarrow/\uparrow) lines. The inset shows the spin polarized Fermi surface, where the nontrivial transformation behavior under C_4 rotations and diagonal mirrors \mathcal{M}_{xy} , $\mathcal{M}_{x\bar{y}}$ becomes apparent.

a symmetric Lieb metal parent state, the ensemble of many-body phases competing with the AM *a priori* has to be assumed to be vast. In particular, since both rotation symmetry and time-reversal symmetry jointly need to be broken to yield an AM transition, any charge-type nematic order or isotropic magnetic order has to be considered on equal footing in order to reach substantiated model evidence. Therefore, an unbiased and general assessment of the many-body instabilities is required to avoid any *a priori* (mean-field) bias. Under these circumstances, the FRG in its optimized static four-point truncated unity approximation (TUFRG) [40–43] is well-established to predict ordering propensities in an efficient manner [44] (see SM [35] for details). Throughout the FRG flow, high-energy modes in all diagrammatic channels are integrated out and their (anti-) screening is incorporated into the resulting effective low-energy theory. Thereby, single-particle features like sublattice polarization and quantum geometry are imprinted into the interaction and may lead to non-trivial transformation behavior of the correlated many-body state under space group operations. We assume the kinetic energy scale, i.e., the electronic bandwidth W , to be the dominant energy scale over the interaction scale U , so that the perturbative diagrammatic resummation through the FRG flow equations is appropriate. Indeed, we checked that the FRG produces comparable results in a broad coupling range $U/t = 0.1 \dots 3.8$ (see SM [35]), as presented below.

In the Lieb lattice model (cf. Fig. 1a), we choose the Fermi level at the VHS close to half filling, expecting ordering tendencies to be strongest at points of high DOS. Given the FS geometry shown in Fig. 1c, the FRG flows towards a magnetic instability irrespective of minor changes to the model [35]. The renormalized interaction is dominated by particle-hole nesting contributions with transfer momentum $\mathbf{q} = \mathbf{g}_{1,2} \equiv \Gamma$, with $\mathbf{g}_{1,2}$ reciprocal lattice vectors. Such “ferromagnetic” (disre-

garding sublattice structure) fluctuations have previously been ascribed to the Lieb lattice’s non-trivial quantum-geometry [45], which is captured by TUFRG. Figure 2a presents a real-space picture of the magnetic order parameter Δ , which has been found to be stable at the mean-field level [33]. In momentum space, its d -wave transformation behavior (B_1 irreducible representation of C_{4v}) becomes apparent, i.e.,

$$\hat{\Delta}(\mathbf{k}) = \hat{\sigma}_z \Delta_M [\cos(k_x) - \cos(k_y)], \quad (2)$$

with Δ_M representing the magnitude and $\hat{\sigma}_z$ the Pauli- z matrix in spin space. While the B/C sites feature a sizable spin polarization, the A site does not participate in the magnetic ordering process. The continuous deformation of the Fermi surface at the phase transition (cf. Fig. 2b) in the absence of translation symmetry breaking classifies the state as an $l = 2$ spin Pomeranchuk instability (sPI) [22, 23]. Compared to the original proposal of Pomeranchuk, the Fermi momenta themselves do not exhibit a reduced symmetry; rather, only the spin polarization along the FS acquires a dependence on the Fermi momentum. This implies TRS breaking without Kramers degeneracy, and provides the non-relativistic P -2 spin momentum locking characteristic for d -wave AMs [21].

In the Lieb lattice structure, the absence of a finite magnetisation on the A site is tightly related to the emergence of an AM state [39]. If a site on the trivial Wyckoff position $1a$ contributes to the magnetic order, the intra-unit cell structure of the magnetic ordering vector is bound to the trivial A_1 representation, and a spin-compensated magnetic state can thus only arise from broken translation symmetry, which would result in an AFM-type state. Intuitively, a finite magnetisation on the A site might be expected due to the higher coordination of the $1a$ Wyckoff position, and hence the resulting increased energy gain in the ordered state. Instead, the itinerant nature of the present instability counteracts a gap on the A site by SI. In particular around van-Hove filling, the scattering channels involve only the B and C sites. Notably, magnetization patterns involving the A site are suppressed for $t > t'$ (i.e., the materials-oriented setting, see SM [35]), promoting AM order on the $2c$ positions [46]. In more general terms, the emergence of the AM state is tied to the sublattice structure at the VHS, which persists even in the case of longer-ranged hoppings and interactions [35]. Our results highlight that in the itinerant picture, magnetic ordering on the A site is not suppressed *a priori* by crystal field effects. Instead, the precise nature electronic band structure states at the Fermi level enables SI to percolate into the renormalized interaction, and eventually to favor an AM instability.

Figure 2b demonstrates how the quasiparticle band structure inherits the non-trivial transformation behavior of the $2c$ sites under C_4 rotations and diagonal mirrors \mathcal{M}_{xy} , $\mathcal{M}_{x\bar{y}}$: In addition to the non-relativistic spin-splitting along Γ - X (Γ - Y), the magnetic gap $\Delta(\mathbf{k})$ exhibits symmetry-protected nodal lines along Γ - M . To

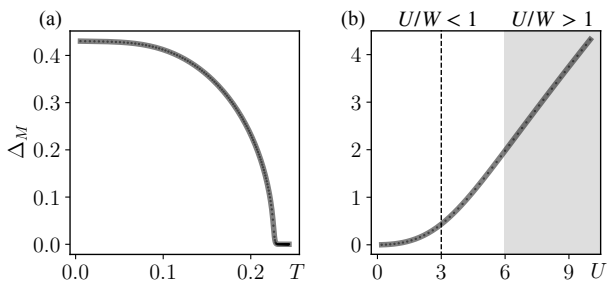


FIG. 3. (a) Size of the altermagnetic order parameter (Δ_M) as a function of temperature (T) for $t' = t/2$ and $U = 3t$, obtained from self-consistent mean-field simulations, showing a clear mean-field phase transition at $T_c/t \approx 0.23$. (b) Value of the magnetic order parameter in the limit of $T = 0$ for U across a large parameter regime. The dashed line indicates $U = 3t$ as used in panel (a).

gain insights on the AM phase transition, we use our FRG result to perform a constrained self-consistent mean-field analysis [35, 47, 48]. We find a second-order transition with Δ smoothly increasing from $T = T_c$ to its maximum value at $T = 0$ (cf. Fig. 3a). At the VHS, where the divergent DOS leads to the largest induced spin gap, we demonstrate that significant values of Δ can be reached: Figure 3b displays the mean-field result for Δ_M as a function of U at zero temperature. Even in the weak to intermediate coupling regime ($U/W < 1$, white region), Δ_M is on the order of t . In turn, the size of the spin splitting δ is readily given by the magnitude of the altermagnetic order parameter Δ_M for $\Delta_M \ll t$ [35] to read

$$\delta(\mathbf{k} = X) = \begin{cases} 2\Delta_M & \text{for the central band,} \\ \Delta_M |1 \pm \mu_A/t| & \text{for the outer bands.} \end{cases} \quad (3)$$

Facing current insecurities about how a theoretically anticipated AM spin splitting scale might relate to the actual splitting scale resolved in experiment, this result encourages the conjecture that AM order resulting from an AM phase transition might not share the big crystal field anisotropy scales, but could still be competitive or even superior in terms of the reachable AM spin splitting.

Discussion—We show how an itinerant electronic Fermi surface instability mechanism can lead to an altermagnetic phase transition. Instead of the conventional hierarchy in altermagnetic materials, where a high-energy crystal field effect precedes magnetic ordering at lower energy scales, our approach makes use of the sublattice texture imprinted into electronic correlations through the Fermi level. As a consequence, only some of the degrees of freedom are selected in the formation of a magnetic state, eventually leading to a spin Pomeranchuk instability. In the ordered phase, the quasiparticle band structure displays features known from altermagnets, i.e., non-relativistic spin splitting with net zero magnetization in the absence of translation symmetry breaking. We illustrate the itinerant mechanism through the example of a Hubbard model on the Lieb lattice. By means of the

functional renormalization group, we obtain its weak coupling instabilities and find a prominent tendency towards an $l = 2$ (d -wave) spin Pomeranchuk order. Notably, the crystal structure does not fall into the classification of altermagnets [39, 49–51]. Instead, sublattice interference leads to selective site participation in the magnetic order. Our obtained magnetization pattern then is equivalent to the P -2 altermagnetic state featured in toy models of RuO_2 [20, 39].

The absence of altermagnetic signatures in RuO_2 [52, 53] as well as MnF_2 [54] candidate materials is remarkable in face of an expectation of large AM energy scale from mean field theory. This might point to a substantial screening effect so far overlooked in the hierarchical, scale-separated symmetry breaking mechanism of local moment AM setups, deserving further investigation. In addition, Ref. [55] demonstrates that altermagnetic *metals* are difficult to find assuming hierarchical symmetry breaking. In this context, the lack of scale separation embodied by our AM mechanism establishes a notable difference, which might bring about beneficial conditions for AM order and its descendant spin splitting. We expect our itinerant AM formation principle to unlock new altermagnetic states in crystallographic geometries outside the conventional classification of altermagnets presented in Refs. [39, 49–51], given the abundance of sublattice interference in various two- and three-dimensional lattices [26]. Since our AM mechanism offers a direct transition from a metallic to an altermagnetic state, it can be probed by, e.g., spin-dependent scanning tunneling microscopy or angle-resolved photoemission spectroscopy. Some candidate systems include covalent organic systems [56], metal-organic frameworks [57], and optical lattices [35]. Furthermore, the approach presented here is not restricted to collinear AM order, but can likewise be applied in the context of non-collinear altermagnetism [58].

Note added—Upon completion of this work, we became aware of an independent work by Li *et. al.* [59], which explores altermagnetism in the Emery model for cuprates. Their and our model relate to each other in the extreme parameter regime $\mu_A \ll 0$.

Acknowledgments—We thank R. Samajdar and T. Müller for useful discussions. M. D. thanks the group of S. Huber at ETH Zürich for their hospitality. This work is supported by the Deutsche Forschungsgemeinschaft (DFG, German Research Foundation) through Project-ID 258499086 – SFB 1170 and through the Würzburg-Dresden Cluster of Excellence on Complexity and Topology in Quantum Matter – ct.qmat Project-ID 390858490 – EXC 2147. We are grateful for HPC resources provided by the Erlangen National High Performance Computing Center (NHR@FAU) of the Friedrich-Alexander-Universität Erlangen-Nürnberg (FAU), that were used for the FRG calculations. NHR funding is provided by federal and Bavarian state authorities. NHR@FAU hardware is partially funded by the DFG – 440719683.

- [1] O. Perron, Zur theorie der matrices, *Mathematische Annalen* **64**, 248 (1907).
- [2] G. Frobenius, *Über Matrizen aus nicht negativen Elementen*, Preussische Akademie der Wissenschaften Berlin: Sitzungsberichte der Preußischen Akademie der Wissenschaften zu Berlin (Reichsdr., 1912).
- [3] C. Wu, K. Sun, E. Fradkin, and S.-C. Zhang, Fermi liquid instabilities in the spin channel, *Phys. Rev. B* **75**, 115103 (2007).
- [4] M. L. Kiesel, C. Platt, and R. Thomale, Unconventional fermi surface instabilities in the kagome hubbard model, *Phys. Rev. Lett.* **110**, 126405 (2013).
- [5] L. Classen, A. V. Chubukov, C. Honerkamp, and M. M. Scherer, Competing orders at higher-order van hove points, *Phys. Rev. B* **102**, 125141 (2020).
- [6] E. I. Kiselev, M. S. Scheurer, P. Wölfle, and J. Schmalian, Limits on dynamically generated spin-orbit coupling: Absence of $l = 1$ pomeranchuk instabilities in metals, *Phys. Rev. B* **95**, 125122 (2017).
- [7] Y.-M. Wu, A. Klein, and A. V. Chubukov, Conditions for $l = 1$ pomeranchuk instability in a fermi liquid, *Phys. Rev. B* **97**, 165101 (2018).
- [8] S. Hayami, Y. Yanagi, and H. Kusunose, Momentum-dependent spin splitting by collinear antiferromagnetic ordering, *Journal of the Physical Society of Japan* **88**, 123702 (2019), <https://doi.org/10.7566/JPSJ.88.123702>.
- [9] L. Šmejkal, R. González-Hernández, T. Jungwirth, and J. Sinova, Crystal time-reversal symmetry breaking and spontaneous hall effect in collinear antiferromagnets, *Science Advances* **6**, eaaz8809 (2020), <https://www.science.org/doi/pdf/10.1126/sciadv.aaz8809>.
- [10] L.-D. Yuan, Z. Wang, J.-W. Luo, E. I. Rashba, and A. Zunger, Giant momentum-dependent spin splitting in centrosymmetric low- z antiferromagnets, *Phys. Rev. B* **102**, 014422 (2020).
- [11] H.-Y. Ma, M. Hu, N. Li, J. Liu, W. Yao, J.-F. Jia, and J. Liu, Multifunctional antiferromagnetic materials with giant piezomagnetism and noncollinear spin current, *Nature Communications* **12**, 2846 (2021).
- [12] I. I. Mazin, K. Koepernik, M. D. Johannes, R. González-Hernández, and L. Šmejkal, Prediction of unconventional magnetism in doped FeSb_2 , *Proceedings of the National Academy of Sciences* **118**, e2108924118 (2021), <https://www.pnas.org/doi/pdf/10.1073/pnas.2108924118>.
- [13] R. Tamang, S. Gurung, D. P. Rai, S. Brahimi, and S. Lounis, Newly discovered magnetic phase: A brief review on altermagnets (2024), [arXiv:2412.05377 \[cond-mat.str-el\]](https://arxiv.org/abs/2412.05377).
- [14] R. González-Hernández, L. Šmejkal, K. Výborný, Y. Yahagi, J. Sinova, T. c. v. Jungwirth, and J. Železný, Efficient electrical spin splitter based on nonrelativistic collinear antiferromagnetism, *Phys. Rev. Lett.* **126**, 127701 (2021).
- [15] D.-F. Shao, S.-H. Zhang, M. Li, C.-B. Eom, and E. Y. Tsymbal, Spin-neutral currents for spintronics, *Nature Communications* **12**, 7061 (2021).
- [16] L. Šmejkal, A. B. Hellenes, R. González-Hernández, J. Sinova, and T. Jungwirth, Giant and tunneling magnetoresistance in unconventional collinear antiferromagnets with nonrelativistic spin-momentum coupling, *Phys. Rev. X* **12**, 011028 (2022).
- [17] Y. Guo, X. Zhang, Z. Huang, J. Chen, Z. Luo, J. Zhang, J. Li, Z. Zhang, J. Zhao, X. Han, and H. Wu, Quantum materials for spintronic applications, *npj Spintronics* **2**, 36 (2024).
- [18] S. Zeng and Y.-J. Zhao, Description of two-dimensional altermagnetism: Categorization using spin group theory, *Phys. Rev. B* **110**, 054406 (2024).
- [19] S.-W. Cheong and F.-T. Huang, Altermagnetism classification (2024), [arXiv:2409.20456 \[cond-mat.mtrl-sci\]](https://arxiv.org/abs/2409.20456).
- [20] L. Šmejkal, J. Sinova, and T. Jungwirth, Emerging research landscape of altermagnetism, *Phys. Rev. X* **12**, 040501 (2022).
- [21] L. Šmejkal, J. Sinova, and T. Jungwirth, Beyond conventional ferromagnetism and antiferromagnetism: A phase with nonrelativistic spin and crystal rotation symmetry, *Phys. Rev. X* **12**, 031042 (2022).
- [22] I. I. Pomeranchuk, On the stability of the fermi liquid, *Sov. Phys. JETP* **8**, 361 (1958).
- [23] A. V. Chubukov, A. Klein, and D. L. Maslov, Fermi-liquid theory and pomeranchuk instabilities: Fundamentals and new developments, *Journal of Experimental and Theoretical Physics* **127**, 826 (2018).
- [24] V. Leeb, A. Mook, L. Šmejkal, and J. Knolle, Spontaneous formation of altermagnetism from orbital ordering, *Phys. Rev. Lett.* **132**, 236701 (2024).
- [25] S. Giuli, C. Mejuto-Zaera, and M. Capone, Altermagnetism from interaction-driven itinerant magnetism (2024), [arXiv:2410.00909 \[cond-mat.str-el\]](https://arxiv.org/abs/2410.00909).
- [26] Y.-P. Lin, Sublattice polarization from destructive interference on common lattices (2024), [arXiv:2406.02671 \[cond-mat.mes-hall\]](https://arxiv.org/abs/2406.02671).
- [27] M. L. Kiesel and R. Thomale, Sublattice interference in the kagome hubbard model, *Phys. Rev. B* **86**, 121105 (2012).
- [28] W. Jiang, M. Kang, H. Huang, H. Xu, T. Low, and F. Liu, Topological band evolution between lieb and kagome lattices, *Phys. Rev. B* **99**, 125131 (2019).
- [29] M. Salmhofer and C. Honerkamp, Fermionic Renormalization Group Flows: Technique and Theory, *Progress of Theoretical Physics* **105**, 1 (2001), <https://academic.oup.com/ptp/article-pdf/105/1/1/5164880/105-1-1.pdf>.
- [30] W. Metzner, M. Salmhofer, C. Honerkamp, V. Meden, and K. Schönhammer, Functional renormalization group approach to correlated fermion systems, *Rev. Mod. Phys.* **84**, 299 (2012).
- [31] C. Platt, W. Hanke, and R. Thomale, Functional renormalization group for multi-orbital fermi surface instabilities, *Advances in Physics* **62**, 453 (2013), <https://doi.org/10.1080/00018732.2013.862020>.
- [32] N. Dupuis, L. Canet, A. Eichhorn, W. Metzner, J. Pawłowski, M. Tissier, and N. Wschebor, The nonperturbative functional renormalization group and its applications, *Physics Reports* **910**, 1 (2021), the nonperturbative functional renormalization group and its applications.
- [33] W.-F. Tsai, C. Fang, H. Yao, and J. Hu, Interaction-driven topological and nematic phases on the lieb lattice, *New Journal of Physics* **17**, 055016 (2015).
- [34] V. J. Emery, Theory of high- T_c superconductivity in oxides, *Phys. Rev. Lett.* **58**, 2794 (1987).
- [35] Supplementary Material published at [\[url will be](#)

- inserted by publisher] with a discussion on (i) the sublattice content of van-Hove singularity, (ii) an effective model for the B/C sites, (iii) details on the TUFGRG calculations and mean-field post-processing, (iv) stability of the AM phase against various model perturbations, (v) a symmetry classification of the AM order parameter, (vi) the size of the spin splitting, and (vii) a realization of the t - t' Lieb lattice model in optical lattices. The SM includes Refs. [60–67].
- [36] X. Wu, T. Schwemmer, T. Müller, A. Consiglio, G. Sangiovanni, D. Di Sante, Y. Iqbal, W. Hanke, A. P. Schnyder, M. M. Denner, M. H. Fischer, T. Neupert, and R. Thomale, Nature of unconventional pairing in the kagome superconductors av_3sb_5 ($a = K, Rb, Cs$), *Phys. Rev. Lett.* **127**, 177001 (2021).
- [37] Y. Hu, X. Wu, B. R. Ortiz, S. Ju, X. Han, J. Ma, N. C. Plumb, M. Radovic, R. Thomale, S. D. Wilson, A. P. Schnyder, and M. Shi, Rich nature of van hove singularities in kagome superconductor csv_3sb_5 , *Nature Communications* **13**, 2220 (2022).
- [38] M. Kang, S. Fang, J.-K. Kim, B. R. Ortiz, S. H. Ryu, J. Kim, J. Yoo, G. Sangiovanni, D. Di Sante, B.-G. Park, C. Jozwiak, A. Bostwick, E. Rotenberg, E. Kaxiras, S. D. Wilson, J.-H. Park, and R. Comin, Twofold van hove singularity and origin of charge order in topological kagome superconductor csv_3sb_5 , *Nature Physics* **18**, 301 (2022).
- [39] M. Roig, A. Kreisel, Y. Yu, B. M. Andersen, and D. F. Agterberg, Minimal models for altermagnetism, *Phys. Rev. B* **110**, 144412 (2024).
- [40] C. Husemann and M. Salmhofer, Efficient parametrization of the vertex function, Ω scheme, and the t, t' Hubbard model at van Hove filling, *Phys. Rev. B* **79**, 195125 (2009).
- [41] J. Lichtenstein, D. Sánchez de la Peña, D. Rohe, E. Di Napoli, C. Honerkamp, and S. Maier, High-performance functional renormalization group calculations for interacting fermions, *Computer Physics Communications* **213**, 100 (2017).
- [42] J. B. Profe and D. M. Kennes, TU^2 FRG: a scalable approach for truncated unity functional renormalization group in generic fermionic models, *The European Physical Journal B* **95**, 60 (2022).
- [43] J. Beyer, J. B. Profe, and L. Klebl, Reference results for the momentum space functional renormalization group, *The European Physical Journal B* **95**, 65 (2022).
- [44] J. B. Profe, D. M. Kennes, and L. Klebl, divERGE implements various Exact Renormalization Group examples, *SciPost Phys. Codebases*, 26 (2024).
- [45] T. Kitamura, A. Daido, and Y. Yanase, Spin-triplet superconductivity from quantum-geometry-induced ferromagnetic fluctuation, *Phys. Rev. Lett.* **132**, 036001 (2024).
- [46] In the limit $t' = 0$, Lieb's theorem holds, and we expect a finite magnetization. Setting $t' \neq 0$, however, does not allow for the same conclusion, enabling AM order to emerge.
- [47] J. Wang, A. Eberlein, and W. Metzner, Competing order in correlated electron systems made simple: Consistent fusion of functional renormalization and mean-field theory, *Phys. Rev. B* **89**, 121116 (2014).
- [48] S.-J. O, Consistent combination of truncated-unity functional renormalization group and mean-field theory, *Phys. Rev. B* **109**, 205118 (2024).
- [49] Y. Guo, H. Liu, O. Janson, I. C. Fulga, J. van den Brink, and J. I. Facio, Spin-split collinear antiferromagnets: A large-scale ab-initio study, *Materials Today Physics* **32**, 100991 (2023).
- [50] C.-C. Wei, E. Lawrence, A. Tran, and H. Ji, Crystal chemistry and design principles of altermagnets, *ACS Organic & Inorganic Au* [10.1021/acsorginorgau.4c00064](https://doi.org/10.1021/acsorginorgau.4c00064) (2024).
- [51] A. Smolyanyuk, L. Šmejkal, and I. I. Mazin, A tool to check whether a symmetry-compensated collinear magnetic material is antiferro- or altermagnetic, *SciPost Phys. Codebases*, 30 (2024).
- [52] J. Liu, J. Zhan, T. Li, J. Liu, S. Cheng, Y. Shi, L. Deng, M. Zhang, C. Li, J. Ding, Q. Jiang, M. Ye, Z. Liu, Z. Jiang, S. Wang, Q. Li, Y. Xie, Y. Wang, S. Qiao, J. Wen, Y. Sun, and D. Shen, Absence of altermagnetic spin splitting character in rutile oxide ruo_2 , *Phys. Rev. Lett.* **133**, 176401 (2024).
- [53] D. T. Plouff, L. Scheuer, S. Shrestha, W. Wu, N. J. Parvez, S. Bhatt, X. Wang, L. Gundlach, M. B. Jungfleisch, and J. Q. Xiao, Revisiting altermagnetism in ruo_2 : a study of laser-pulse induced charge dynamics by time-domain terahertz spectroscopy (2024), [arXiv:2412.11240](https://arxiv.org/abs/2412.11240) [cond-mat.mtrl-sci].
- [54] V. C. Morano, Z. Maesen, S. E. Nikitin, J. Lass, D. G. Mazzone, and O. Zaharko, Absence of altermagnetic magnon band splitting in mnf_2 (2024), [arXiv:2412.03545](https://arxiv.org/abs/2412.03545) [cond-mat.str-el].
- [55] X. Wan, S. Mandal, Y. Guo, and K. Haule, High-throughput search for metallic altermagnets by embedded dynamical mean field theory (2024), [arXiv:2412.10356](https://arxiv.org/abs/2412.10356) [cond-mat.mtrl-sci].
- [56] B. Cui, X. Zheng, J. Wang, D. Liu, S. Xie, and B. Huang, Realization of lieb lattice in covalent-organic frameworks with tunable topology and magnetism, *Nature Communications* **11**, 66 (2020).
- [57] Y. Che, H. Lv, X. Wu, and J. Yang, Realizing altermagnetism in two-dimensional metal-organic framework semiconductors with electric-field-controlled anisotropic spin current, *Chem. Sci.* **15**, 13853 (2024).
- [58] S.-W. Cheong and F.-T. Huang, Altermagnetism with non-collinear spins, *npj Quantum Materials* **9**, 13 (2024).
- [59] Y. Li, V. Leeb, K. Wohlfeld, R. Valentí, and J. Knolle, d -wave magnetism in cuprates from oxygen moments (2024), [arXiv:2412.11922](https://arxiv.org/abs/2412.11922) [cond-mat.str-el].
- [60] C. Karrasch, *The functional renormalization group for zero-dimensional quantum systems in and out of equilibrium*, Ph.D. thesis, Aachen (2010), aachen, Techn. Hochsch., Diss., 2010.
- [61] D. Kalkstein and P. Soven, A green's function theory of surface states, *Surface Science* **26**, 85 (1971).
- [62] M. P. Lopez Sancho, J. M. Lopez Sancho, J. M. L. Sancho, and J. Rubio, Highly convergent schemes for the calculation of bulk and surface green functions, *Journal of Physics F: Metal Physics* **15**, 851 (1985).
- [63] J. Reiss, D. Rohe, and W. Metzner, Renormalized mean-field analysis of antiferromagnetism and d -wave superconductivity in the two-dimensional hubbard model, *Phys. Rev. B* **75**, 075110 (2007).
- [64] M. Dürrnagel, J. Beyer, R. Thomale, and T. Schwemmer, Unconventional superconductivity from weak coupling, *The European Physical Journal B* **95**, 112 (2022).
- [65] M. Di Liberto, A. Hemmerich, and C. Morais Smith, Topological varma superfluid in optical lattices, *Phys. Rev. Lett.* **117**, 163001 (2016).

- [66] R. Shen, L. B. Shao, B. Wang, and D. Y. Xing, Single dirac cone with a flat band touching on line-centered-square optical lattices, [Phys. Rev. B **81**, 041410 \(2010\)](#).
- [67] J. B. Profe, L. Klebl, F. Grandi, H. Hohmann, M. Dürnagel, T. Schwemmer, R. Thomale, and D. M. Kennes, Kagome hubbard model from a functional renormalization group perspective, [Phys. Rev. Res. **6**, 043078 \(2024\)](#).

Supplementary material: Altermagnetic phase transition in a Lieb metal

Matteo Dürrnagel,^{*} Hendrik Hohmann,^{*} Atanu Maity, Jannis Seufert, Michael Klett, Lennart Klebl, and Ronny Thomale[†]

*Institut für Theoretische Physik und Astrophysik and Würzburg-Dresden Cluster of Excellence ct.qmat,
Universität Würzburg, 97074 Würzburg, Germany*

(Dated: December 20, 2024)

CONTENTS

S1. Sublattice content of the low-energy van-Hove singularity	S1
S2. Effective model for the B/C sites	S2
S3. Details on the (TU)FRG calculations	S2
A. Static four-point TUFGR	S2
B. Numerical details	S3
C. Mean-field altermagnetic phase transition from FRG	S3
S4. Stability analysis of the altermagnetic phase	S5
A. Interaction parameters	S5
B. Kinetic parameters	S6
C. Dominance of the altermagnetic order parameter	S6
S5. Symmetry classification of the d -wave altermagnetic order	S7
S6. Size of the non-relativistic spin splitting	S8
S7. Realization in an optical lattice	S9

S1. SUBLATTICE CONTENT OF THE LOW-ENERGY VAN-HOVE SINGULARITY

Transforming the kinetic part of the Hamiltonian [cf. Eq. (1)] to momentum space, we obtain a matrix in sublattice space (A, B, C) for each BZ momentum \mathbf{k} :

$$H(\mathbf{k}) = \begin{pmatrix} -\mu_A & A_{k_x} & A_{k_y} \\ A_{k_x} & 0 & B_{\mathbf{k}} \\ A_{k_y} & B_{\mathbf{k}} & 0 \end{pmatrix}. \quad (\text{S1})$$

Here, we dropped its spin dependence due to $SU(2)$ symmetry. Without loss of generality, we set $\mu_B = \mu_C = 0$. The coefficients of Eq. (S1) are given as

$$A_{k_x} = 2t \cos\left(\frac{k_x}{2}\right), \quad A_{k_y} = 2t \cos\left(\frac{k_x}{2}\right), \quad B_{\mathbf{k}} = 4t' \cos\left(\frac{k_x}{2}\right) \cos\left(\frac{k_y}{2}\right). \quad (\text{S2})$$

From the functional form of Eqs. (S1) and (S2) it is directly evident that a zero energy state persists at the zone boundary (in the presence of arbitrary t') since there, $\cos(k_x/2) = 0 \vee \cos(k_y/2) = 0$. Along a zone boundary path,

^{*} These authors contributed equally.

[†] ronny.thomale@uni-wuerzburg.de

e.g., M - X , the Hamiltonian acquires the simple form

$$H(\mathbf{k}) = \begin{pmatrix} -\mu_A & 0 & 2t \cos(k_y/2) \\ 0 & 0 & 0 \\ 2t \cos(k_y/2) & 0 & 0 \end{pmatrix}, \quad (\text{S3})$$

and the polarization of the zero mode eigenstate in the B sublattice is directly apparent from the matrix form of Eq. (S3). At $M = (\pi, \pi)$, this is a zero triple state for $\mu_A = 0$ and evolves into a quadratic band touching point at finite μ_A as the Dirac cone is gapped out by the Semenov-like mass term in analogy to the Honeycomb lattice [33].

Adding additional hoppings beyond second nearest neighbor (e.g. diagonal B - B and C - C hoppings across the plaquettes) leads to a warping of the Fermi surface in correspondence to the square lattice Hubbard model with NNN hoppings. While this reduces the nesting features of the FS and leads to a reduction of the critical temperature, the orbital character and nesting vector of the VHS persists and continues to support the altermagnetic phase.

S2. EFFECTIVE MODEL FOR THE B/C SITES

Starting with the Hamiltonian defined in Eq. (S1), we can write it as a block matrix in sublattice space:

$$H = \begin{pmatrix} H_A & T^\dagger \\ T & H_{BC} \end{pmatrix}. \quad (\text{S4})$$

The corresponding free Greens functions for the two subspaces are given by $\mathcal{G}_{A,BC}^0 = (i\omega - H_{A,BC})^{-1}$. We build an effective model for the B and C sublattices by treating $T \propto t$ as perturbation. Note that in our model, however, t is not a small parameter and therefore a perturbative treatment is not justified *a priori*. The effective BC subspace Green's function then reads [60–62]

$$\mathcal{G}_{BC} = \frac{1}{(\mathcal{G}_{BC}^0)^{-1} - \frac{T\mathcal{G}_A^0 T^\dagger}{(\mathcal{G}_{BC}^0)^{-1} - \frac{T\mathcal{G}_A^0 T^\dagger}{(\mathcal{G}_{BC}^0)^{-1} - \dots}}} \approx \frac{1}{i\omega - H_{BC} - T\mathcal{G}_A^0 T^\dagger} \equiv \frac{1}{i\omega - H_{BC} - \Sigma_{BC}}, \quad (\text{S5})$$

where the approximation corresponds to a truncation of the continued fraction at leading order. The (hybridization) self-energy Σ_{BC} is therefore given as

$$\Sigma_{BC}(i\omega, \mathbf{k}) = \frac{4t^2}{i\omega + \mu_A} \begin{pmatrix} \cos^2(k_x/2) & \cos(k_x/2) \cos(k_y/2) \\ \cos(k_x/2) \cos(k_y/2) & \cos^2(k_y/2) \end{pmatrix}, \quad (\text{S6})$$

which we can recast into an effective Hamiltonian in the zero frequency limit:

$$H_{BC}^{\text{eff}}(\mathbf{k}) = H_{BC}(\mathbf{k}) + \Sigma_{BC}(0, \mathbf{k}) = \begin{pmatrix} 4Z \cos^2(k_x/2) & 4(t' + Z) \cos(k_x/2) \cos(k_y/2) \\ 4(t' + Z) \cos(k_x/2) \cos(k_y/2) & 4Z \cos^2(k_y/2) \end{pmatrix}, \quad (\text{S7})$$

where we defined the expansion parameter $Z = t^2/\mu_A$ for brevity. Rotating the coordinate system by 45° ($2q_x = k_x + k_y$, $2q_y = k_y - k_x$) aligns the BC plaquette with the x - y directions, which results in

$$H_{BC}^{\text{eff}}(\mathbf{q}) = \begin{pmatrix} 2Z(1 + \cos(q_x/2 + q_y/2)) & (t' + Z)(\cos(q_x/2) + \cos(q_y/2)) \\ (t' + Z)(\cos(q_x/2) + \cos(q_y/2)) & 2Z(1 + \cos(q_x/2 - q_y/2)) \end{pmatrix}. \quad (\text{S8})$$

The second order processes in t (first order in Z) breaks the local C_4 symmetry around the B and C sites by introducing direction dependent hoppings on the Hamiltonian's diagonal. This scenario is reminiscent of the effective models for AM in RuO₂ (compare e.g. Eq. (17) in Ref. [39]).

S3. DETAILS ON THE (TU)FRG CALCULATIONS

A. Static four-point TUFrg

We use the FRG in its static four-point approximation. This means that we disregard all higher (six, eight, ...) point interaction vertices as well as self-energies in the expansion of the vertex generating functional [30]. The

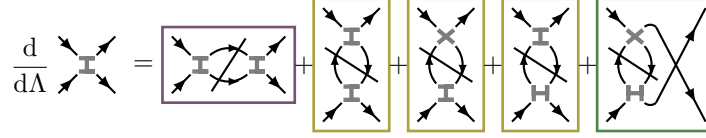


FIG. S1. Diagrammatic representation of static four-point FRG. We group the three channels by color: particle-particle channel (P , purple), direct particle-hole channel (D , yellow), and crossed particle-hole channel (C , green). Spin is conserved along the short edge of each vertex.

resulting diagrammatic structure of the FRG flow equations is visualized in Fig. S1. In addition to the truncation of the number of fermionic fields participating in possible interactions, we disregard the frequency dependence of all vertices. This approximation has proven useful when characterizing ordering propensities of weakly to intermediately interacting electron systems [29]. As the four-point vertices are still complicated objects, they are routinely compressed in numerical simulations: The primary (bosonic) momentum is resolved in momentum space, while the secondary (fermionic) momenta are treated in a truncated real-space basis. This coins the “truncated unity” approximation of FRG, i.e., TUFGR [40–43].

B. Numerical details

The FRG calculations were performed with the TUFGR backend of the divERGe library, making use of the sharp frequency cutoff as it boosts numerical performance [44]. We employed a 30×30 mesh for the bosonic momenta of the vertices, with an additional refinement of 51×51 for the integration of the loop. The form-factor cutoff distance is chosen as 2.51 in units of lattice vector length. We check for convergence by calculating selected points in parameter space with increased number of momentum points and form-factor cutoff (42×42 , refinement: 81×81 , formfactor cutoff: 3.51). We employed the adaptive Euler integrator of the divERGe library with default parameters. Calculations displayed in the main part of this work were obtained for nearest ($t = 1$) and next-nearest neighbor hopping ($t' = 0.5$), and equal onsite interactions and chemical potentials on the three sublattices ($U = 1$, $\mu_i = 0$) as given by the interaction Hamiltonian in Eq. (1) of the main text.

C. Mean-field altermagnetic phase transition from FRG

The truncation of the FRG flow equations breaks down when approaching a phase transition and results in a divergence of the two-particle vertex. Investigating the symmetry breaking beyond the phase transition predicted by FRG can be achieved by formulating an effective mean-field (MF) theory. To bridge the non-analytic behaviour of the FRG flow at the phase transition and smoothly connect the ordered state with the high temperature phase, we follow the procedure outlined in Refs. [47, 48]: Close to the phase transition, the divergence stems from the ladder series of the diverging channel and is only marginally altered by cross channel projections. To obtain an appropriate bare interaction V_{MF} for MF treatment (at scale $\Lambda_{\text{MF}} \gtrsim \Lambda_C$), one can extrapolate this regime to high energies. In practice, we ‘reverse’ the ladder resummation in the divergent channel over the full range of renormalization group scales (here given in the magnetic channel):

$$\Gamma^{\Lambda_{\text{MF}}}(14, 32) = V_{\text{MF}}(14, 32) - \sum_{1'2'3'4'} V_{\text{MF}}(14, 3'2') L(3'2', 1'4') \Gamma^{\Lambda_{\text{MF}}}(1'4', 32) \quad (\text{S9})$$

with the appropriate bare susceptibility $L(12,34)$. Here, all quantum numbers are combined in roman numeral multi-indices. Inverting the above equation defines the starting point of the MF treatment. By construction, a subsequent MF analysis will yield the correct MF state.

In the present case, the AM symmetry breaking is directly triggered by the bare interaction: Even without cross-channel feedback, an RPA resummation in the magnetic channel yields the same AM instability (as evidenced by the pronounced peak in the particle-hole susceptibility spectrum displayed in Fig. S5). So the inversion of an RPA ladder outlined above results in the *actual* bare $V_{\text{MF}} \equiv U$. We can thus equivalently employ an MF decomposition of the bare Hamiltonian [cf. Eq. (1)]. To derive the self-consistent MF equations we calculate the free energy at fixed total particle number n_{tot} :

$$F = -\frac{1}{\beta} \ln(\mathcal{Z}) + \mu n_{\text{tot}} = -\frac{1}{\beta} \ln \left(\int \mathcal{D}[\psi, \bar{\psi}] e^{-S(\psi, \bar{\psi})} \right) + \mu n_{\text{tot}}, \quad (\text{S10})$$

with the action S given by

$$S(\psi, \bar{\psi}) = S_0(\psi, \bar{\psi}) + S_I(\psi, \bar{\psi}) = \frac{1}{N} \sum_{kss'o_1o_2} \bar{\psi}_{k_{o_1s}} (-i\omega_n \delta_{ss'} \delta_{o_1o_2} + H_{o_1o_2}^0(\mathbf{k}) \delta_{ss'}) \psi_{k_{o_2s'}} + \frac{U}{N^2} \sum_{k_iss'o} \bar{\psi}_{k_1os} \bar{\psi}_{k_2os'} \psi_{k_3os'} \psi_{k_1+k_2-k_3os}, \quad (\text{S11})$$

where $k = (\mathbf{k}, \omega_n)$ and $H^0(\mathbf{k})$ the non-interacting Hamiltonian given in Eq. (S1). We decouple the interaction with a Hubbard-Stratonovich transformation and constrain the bosonic fields to the static order parameter of the FRG calculation:

$$\Delta_{o_1o_2} = \frac{U}{N} \sum_{kss'} \langle \bar{\psi}_{k_{o_1s}} \sigma_z^{ss'} \psi_{k_{o_2s'}} \rangle = \begin{pmatrix} 0 & 0 & 0 \\ 0 & \Delta_M & 0 \\ 0 & 0 & -\Delta_M \end{pmatrix}, \quad (\text{S12})$$

where the Pauli- z matrix σ_z fixes the magnetization axis without loss of generality. Neglecting fluctuations of around the MF state, we obtain a quadratic action that reads

$$S(\psi, \bar{\psi}) = \sum_{k_{o_1o_2ss'}} \bar{\psi}_{k_{o_1s}} (-i\omega_n \delta_{ss'} \delta_{o_1o_2} + H_{o_1o_2ss'}^0 + \Delta_{o_1o_2} \sigma_z^{ss'}) \psi_{k_{o_2s'}} - \frac{1}{U} \sum_o \Delta_{oo}^2. \quad (\text{S13})$$

With this effective action, the partition sum Eq. (S10) can be integrated to yield

$$F = \frac{1}{U} \sum_o \Delta_{oo}^2 - \frac{1}{\beta N} \sum_{kn} \ln(1 + e^{-\beta E_{kn}}) + \mu n_{\text{tot}}, \quad (\text{S14})$$

with quasiparticle energies satisfying the eigenvalue equation

$$\det \left(\underbrace{H_{o_1o_2}^0(\mathbf{k}) \delta_{ss'} + \Delta_{o_1o_2} \sigma_z^{ss'}}_{\mathcal{H}(\mathbf{k})} - E_{kn} \delta_{o_1o_2} \delta_{ss'} \right) = 0. \quad (\text{S15})$$

Since the effective Hamiltonian is block diagonal in spin space, we exploit this symmetry: $\Delta_{BB} \sigma_z^{\uparrow\uparrow} = \Delta_{CC} \sigma_z^{\downarrow\downarrow}$. In conjunction with C_{4v} symmetry of the free Hamiltonian ($H^0(\mathbf{k}) = H_{B \leftrightarrow C}^0(C_4 \mathbf{k})$), it becomes evident that the contribution of the spin- \uparrow and \downarrow blocks to the free energy are identical. So we constrain E_{kn} to the eigenvalues of the spin up block $H_{\uparrow\uparrow}(\mathbf{k})$ given by Eq. (S12) and we can simply add a spin factor of 2 to the corresponding term in the free energy.

The gap magnitude Δ_M is chosen such that the free energy Eq. (S14) is minimized, i.e.,

$$\frac{\partial F}{\partial \Delta_M} = \frac{4}{U} \Delta_M + \frac{2}{\beta N} \sum_{kn} \frac{1}{1 + e^{\beta E_{kn}}} \frac{\partial E_{kn}}{\partial \Delta_M} = \frac{4}{U} \Delta_M + \frac{2}{\beta N} \sum_{kn} f(\beta E_{kn}) \frac{\partial E_{kn}}{\partial \Delta_M} = 0. \quad (\text{S16})$$

Applying the matrix identity ($\det(M)^{ii'}$ denotes the minor determinant)

$$\frac{\partial}{\partial x} \det(M) = \sum_{ii'} \frac{\partial M_{ii'}}{\partial x} (-1)^{i-i'} \det(M)^{ii'} \quad (\text{S17})$$

to the eigenvalue problem Eq. (S15), one can express the derivative of the eigenenergies as [63]

$$\frac{\partial E_{kn}}{\partial \Delta_M} = \frac{1}{\sum_o \det(M^n(\mathbf{k}))^{oo}} \sum_{o_1o_2} \frac{\partial \mathcal{H}_{o_1o_2}(\mathbf{k})}{\partial \Delta_M} (-1)^{o_1-o_2} \det(M^n(\mathbf{k}))^{o_1o_2}, \quad (\text{S18})$$

where we defined the matrix $M_{o_1o_2}^n(\mathbf{k}) = \mathcal{H}_{o_1o_2}(\mathbf{k}) - E_{kn} \delta_{o_1o_2}$. Using the shape of the order parameter and inserting the result in Eq. (S16), this gives the final expression for the self-consistent gap equation

$$\Delta_M = -\frac{U}{2N} \sum_{kn} \frac{f(\beta E_{kn})}{\sum_o \det(M^n(\mathbf{k}))^{oo}} \left(\det(M^n(\mathbf{k}))^{BB} - \det(M^n(\mathbf{k}))^{CC} \right). \quad (\text{S19})$$

The solutions for Eq. (S19) depicted in Fig. 3 of the main text were obtained with a Brillouin zone sampling of 2000×2000 \mathbf{k} points.

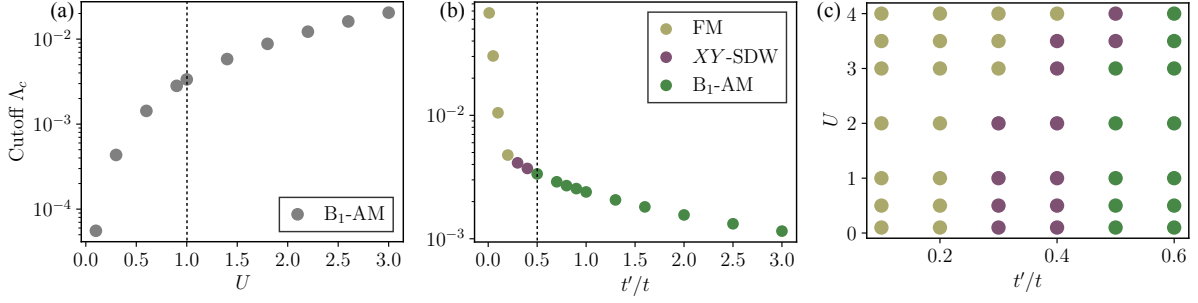


FIG. S2. Critical cutoff scale Λ_c of (a) the proposed AM state for different values of $U_A = U_{B,C}$ at $t' = 0.5$ and (b) competing phases for different values of t' at $U_i = 1$ depicted in Fig.S3. (c) Joint phase diagram the U, t' parameter space. We see that the AM state is stable in a broad parameter regime and extends to relatively large values of interaction.

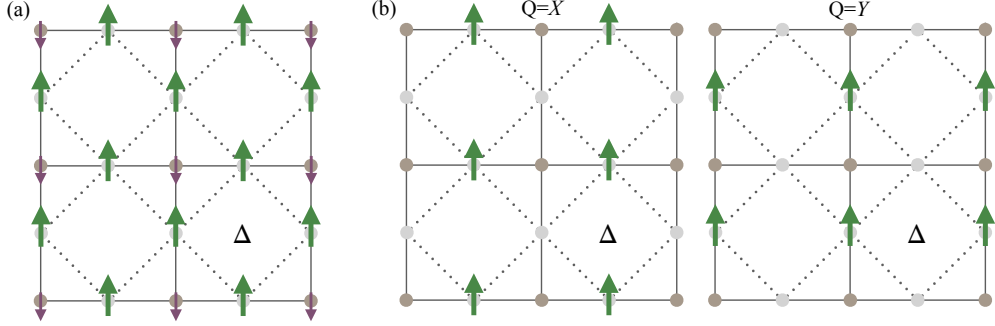


FIG. S3. (a) Ferromagnetic (FM) phase emerging at small t' . As the A site participates in the magnetization process, a slight tendency towards ferrimagnetism can be observed. (b) XY -spin density wave emerging at the interface of FM and AM. At the phase transition, all linear combinations of the twofold degenerate order parameter are allowed solutions of the linearized gap equation.

S4. STABILITY ANALYSIS OF THE ALTERMAGNETIC PHASE

The results shown in the main part of this work were obtained for NN ($t = 1$) and NNN hopping ($t' = 0.5$), and equal onsite interactions and chemical potentials on the three sublattices ($U = 1, \mu_i = 0$) as given by the interaction Hamiltonian in Eq. (1) of the main text. The filling is adjusted such that the t' -induced VHS resides at zero energy. To investigate the resilience of the proposed AM state we consider perturbations in both the kinetic and the interaction part of the simplified Hamiltonian. We find the AM instability being robust against several changes summarized in the following subsections. Unless stated otherwise, the remaining parameters are kept as specified in this paragraph.

A. Interaction parameters

We demonstrate that the proposed AM state remains robust across the entire weak to intermediate coupling regime of onsite interactions $U_A = U_{B,C}$. Figure S2 a shows the critical cutoff scale Λ_c for different values of U . The cutoff scale, being a handle on the critical temperature, increases rapidly with increased coupling strength. Furthermore, we analyze how different onsite interactions on the two types of sublattices affect the stability of the state, i.e. $U_A \neq U_{B,C}$. For fixed $U_{B,C} = 1$ the AM state persists for $U_A = 0 \dots 2.5$.

We additionally allow for longer-ranged interactions, i.e., nearest-neighbor (NN) interactions V and next-nearest-neighbor (NNN) interactions V' . While NN interactions between Wyckoff positions $1a$ and $2c$ have no effect on the AM state up to $V = 0.6$, V' (which couples the B and C sites) drives a B_1 intra-unit cell charge density wave upon exceeding $V' = 0.2$. These results are in agreement with previous mean-field results on the Lieb lattice [33] and are driven by an effect extensively discussed in Hubbard model on the Kagome lattice: Due to the sublattice interference mechanism [27] the system is less likely to form a local magnetization density, since the onsite interaction is partially screened by the sublattice character of states on the FS. Hence, the system has more incentive to ease the NN repulsion by a charge imbalance of the neighbouring sites rather than the onsite repulsion [4, 67].

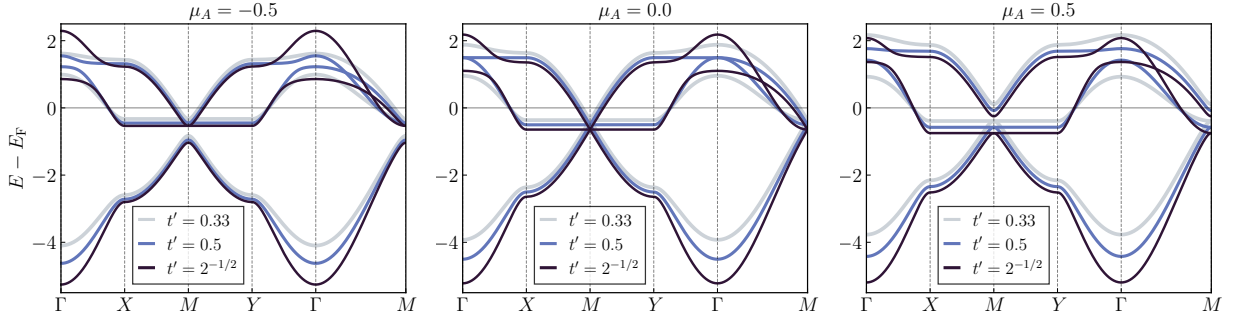


FIG. S4. Band structures for different values of intrinsic detuning $\mu_A \neq \mu_{B,C} = 0.0$ and NNN hopping t' at pristine filling. The sublattice polarized VHS that drives the AM phase transition persists. For $t' \rightarrow 0$ the VHS approaches half filling and the band flattens.

B. Kinetic parameters

Figure S4 displays different values of intrinsic detuning $\mu_A \neq \mu_{B,C} = 0.0$ and NNN hopping t' at pristine filling. The sublattice polarized VHS at the X/Y point persists for arbitrary values of μ_A and arbitrary but finite values of t' as it corresponds to a topologically protected band touching point. This property is reflected in the resilience of the AM phase upon variation of $t' \geq 0.5$ (see Fig. S2b) and $\mu_A = -2.0 \dots 3.0$.

At $U = 1$ and small $t' < 0.3$ the dominant contribution to the leading instability is provided by a ferromagnet (FM) on the B and C sites. The trivial irrep in real space allows for a participation of the central A site in the magnetisation process, which results in a ferrimagnetic phase (Fig. S3a). A degenerate $Q = X, Y$ spin density wave (SDW) resides at the interface between FM and AM order (Fig. S3b). A phase diagram showing the three competing instabilities depending on both U and t' is shown in Fig. S3c. The competition between these three states is already apparent at the bare level as discussed in Section S4C. A sign difference between t and t' does not affect this phenomenology, as it merely inverts the dispersion of the BC band in energy. Small perturbations from even longer-ranged hybridizations, i.e., same-sublattice third nearest-neighbor hoppings t'' , alter the shape of the Fermi surface (FS), resulting in a loss of perfect nesting conditions and, consequently, a suppression of critical scales.

For the given band structure, itinerant phases are generally suppressed for small amounts of hole doping as the DOS rapidly declines (see Fig. 1b). For small amounts of electron doping, the B/C polarized band is still present at the Fermi surface stabilizing the AM phase with tendencies to form the particle-hole condensate at slightly incommensurate momenta. As the logarithmically diverging DOS and perfect nesting scenario is absent at the Fermi level, intermediate interaction values are necessary to obtain the altermagnetic phase in our FRG calculations (e.g., $U_i = 1.4 \dots \geq 2.6$ for $\mu = 0.02$).

C. Dominance of the altermagnetic order parameter

To connect the orbital character of the eigenstates at the VHS with the emergent symmetry breaking, we inspect the bare static particle-hole susceptibility

$$\chi_{o_1 o_2 o_3 o_4}^0(\mathbf{Q}) = - \int_{\text{BZ}} \frac{d\mathbf{k}}{V_{\text{BZ}}} \frac{f(\beta \varepsilon_n(\mathbf{k} + \mathbf{Q})) - f(\beta \varepsilon_m(\mathbf{k}))}{\varepsilon_n(\mathbf{k} + \mathbf{Q}) - \varepsilon_m(\mathbf{k})} M_{\{o_i\}}^{nm}(\mathbf{k}, \mathbf{Q}). \quad (\text{S20})$$

The momentum space integral and Fermi distribution $f(\beta \varepsilon)$ is evaluated on a momentum space mesh in the BZ of volume V_{BZ} and at an inverse temperature β in the implementation described in Ref. [64].

In multi-orbital systems, χ^0 features a dependence not only on the single particle energies $\varepsilon_n(\mathbf{k})$ but also on the orbital-to-band transformations of the electronic eigenstates $u_{o_i}^n(\mathbf{k})$ via

$$M_{\{o_i\}}^{nm}(\mathbf{k}, \mathbf{Q}) = [u_{o_1}^n(\mathbf{k} + \mathbf{Q})]^* [u_{o_2}^m(\mathbf{k})]^* u_{o_3}^n(\mathbf{k} + \mathbf{Q}) u_{o_4}^m(\mathbf{k}). \quad (\text{S21})$$

Since higher energy fluctuations are suppressed by the denominator in Eq. (S20), the largest contribution to the integral is given by the states close to the Fermi level. This introduces an energetic hierarchy to the eigenstates on the bandstructure and one can select the dominant screening channels by placing the Fermi level accordingly. This effect is highlighted in Fig. S5: For the Fermi level at the VHS close to half filling, the bare susceptibility features

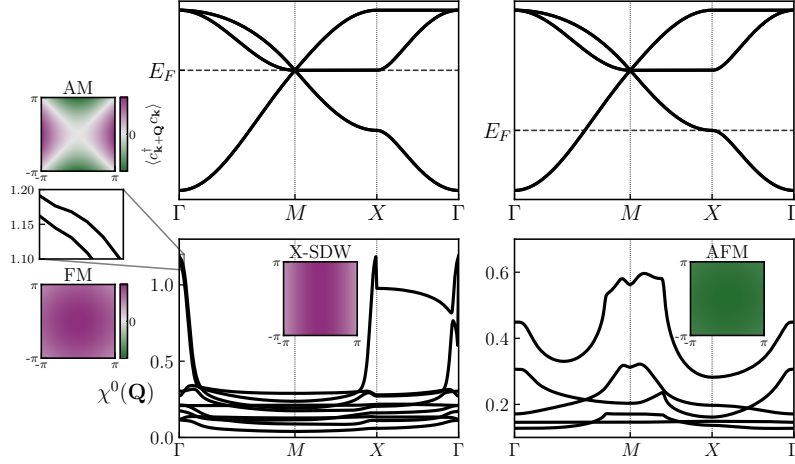


FIG. S5. Bandstructure and eigenvalues of the bare susceptibility at lower VHS (left) and middle VHS (right) for the Hamiltonian in Eq. (1) of the main text for $t = -1$, $t' = 0.5t$ and $\mu_A = 0$. We evaluated the bare susceptibility via Eq. (S20) on a \mathbf{k} -mesh of 2000×2000 and set $\beta = 100/t$. The insets show the eigenvector associated with the leading eigenvalues at distinct \mathbf{Q} values in the whole BZ. We note that ferromagnetic fluctuations are suppressed on the bare level already when doping to the center VHS (left column).

a pronounced peak at Γ and X associated with the dominant FS nesting vectors on the BC derived Fermi sheet. Contrarily, at the lower VHS the eigenstates on the FS are mostly dominated by the A sublattice and the pronounced M nesting displays an AFM spin fluctuation texture.

At the central VHS, the bare susceptibility shows two dominant peaks: While at Γ the susceptibility is guaranteed to feature a local maximum by quantum geometric arguments [45], the relative angular momentum of the resulting particle-hole condensate is determined by the ratio t'/t . NNN hopping (t') mediates a direct AFM coupling between the B and C sites $\propto t'^2$ that is counteracted by a second order FM coupling via the A site of order t^4 . Their competition is directly reflected in the close proximity of the leading spin fluctuation in Fig. S5 at the Γ point. In the t' -dominated regime the associated electronic fluctuations display a clear d -wave altermagnetic character in accordance with the intuitive picture provided in the main text with a subleading FM order (see Fig. S3a). For small t'/t , this hierarchy is inverted resulting in the low energy FM phase in Fig. S2b.

The additional peak at $\mathbf{Q} = X/Y$ corresponds to the dominant Fermi surface nesting vector of the FS at the Lifshitz transition. It is generically disfavored at the bare level compared to the Γ point condensate, since it can not exploit the mixed sublattice contributions directly at the van-Hove point M . However, the destructive interference of the AM and FM fluctuations at $\mathbf{Q} = \Gamma$ promotes an X/Y modulated spin density wave as the dominant magnetic instability in the intermediate t' region (cf. Fig. S2).

S5. SYMMETRY CLASSIFICATION OF THE d -WAVE ALTERMAGNETIC ORDER

Non-relativistic collinear magnetism is generally classified by spin groups [18, 20] described as the direct product: $r_s \times R_s$. Here, r_s refers to the spin only group whose implication on the band structure of collinear magnets is $\epsilon_\sigma(k_x, k_y) = \epsilon_\sigma(-k_x, -k_y)$ regardless of whether the real-space inversion symmetry is present. Here, $r_s = [C_\infty || E] + [\bar{C}_2 C_\infty || E]$ where C_∞ is any rotation around the common spin axis and \bar{C}_2 is the two-fold rotation around the axis perpendicular to the spins combined with spin space inversion. In the notation $[R_i || R_j]$, $R_i(R_j)$ incorporates all the spin (crystallographic) space operations.

In contrast, the non-trivial spin group R_s , which does not contain any elements of r_s , plays a crucial role in determining the non-relativistic spin-split band structure. The group R_s generally comprises pairs of operations acting independently on spin and real space. There are three distinct types of R_s , each corresponding to a specific type of collinear magnet.

1. **Type I:** Denoted by $R_s^I = [E || G]$ where G belongs to a crystallographic Laue group. This type results in complete spin splitting of the band structure, as observed in ferromagnets or ferrimagnets.
2. **Type II:** Denoted by $R_s^{II} = [E || G] + [C_2 || G]$ where C_2 is a spin-inversion operation. This leads to a spin-degenerate band structure, typical of trivial collinear antiferromagnets.

3. Type III: Denoted by $R_s^{III} = [E||H] + [C_2||G - H = A]$ where H is a halving subgroup of G . This type gives rise to the altermagnetic phase, characterized by non-trivial non-relativistic spin splitting in spin-compensated collinear magnets.

The observed phase in this study belongs to the third category. Specifically, the non-trivial spin group is given by $[C_2||A]$ where A includes three symmetry elements \mathcal{M}_{xy} (mirror plane perpendicular to xy plane and passing through $x = y$), $\mathcal{M}_{x\bar{y}}$ (mirror plane perpendicular to xy plane and passing through $x = -y$) and C_4 (C_{4z} rotational axis) that interchanges B and C sublattices:

$$\begin{aligned} [C_2||\mathcal{M}_{xy}] : \epsilon_\sigma(k_x, k_y) &\rightarrow \epsilon_{-\sigma}(k_y, k_x), \\ [C_2||\mathcal{M}_{x\bar{y}}] : \epsilon_\sigma(k_x, k_y) &\rightarrow \epsilon_{-\sigma}(-k_y, -k_x), \\ [C_2||C_4] : \epsilon_\sigma(k_x, k_y) &\rightarrow \epsilon_{-\sigma}(-k_y, k_x). \end{aligned} \quad (\text{S22})$$

The first two equations ensure the symmetry protected spin degeneracy along the lines $k_x = \pm k_y$, i.e., along the segment Γ - M .

S6. SIZE OF THE NON-RELATIVISTIC SPIN SPLITTING

In the magnetic state, spin degeneracy is lifted and the overall Hamiltonian can be written in a block diagonal fashion

$$\mathcal{H}(\mathbf{k}) = \begin{pmatrix} \mathcal{H}_{\uparrow\uparrow}(\mathbf{k}) & 0 \\ 0 & \mathcal{H}_{\downarrow\downarrow}(\mathbf{k}) \end{pmatrix}. \quad (\text{S23})$$

Even in the presence of magnetic ordering the two spin blocks decouple and we can obtain the eigenvalues of the spin- \uparrow polarized bands by diagonalization of the matrix

$$\mathcal{H}_{\uparrow\uparrow}(\mathbf{k}) = \begin{pmatrix} -\mu_A & A_{k_x} & A_{k_y} \\ A_{k_x} & \Delta_M & B_k \\ A_{k_y} & B_k & -\Delta_M \end{pmatrix} \quad (\text{S24})$$

with Δ_M ($-\Delta_M$) the spin polarization on the B (C) sublattice. The corresponding eigenvalues for spin- \downarrow are obtained by flipping the sign: $\Delta_M \rightarrow -\Delta_M$.

To assess the size of the spin splitting we recall that the magnetic order parameter transforms in a B_1 irrep of C_{4v} , i.e., the spin splitting is to lowest order $\propto \cos(k_x) - \cos(k_y)$ [39]. Hence, the maximum value of the spin splitting is expected at the X/Y points. We therefore investigate the Hamiltonian at $X = (\pi, 0)$,

$$\mathcal{H}_{\uparrow\uparrow}(\mathbf{k} = X) = \begin{pmatrix} -\mu_A & 0 & 2t \\ 0 & \Delta_M & 0 \\ 2t & 0 & -\Delta_M \end{pmatrix}, \quad (\text{S25})$$

to quantify the spin splitting. The eigenvalues of this matrix as well as its spin-down counterpart are given by

$$\begin{aligned} E_{\uparrow}^1(X) &= -\Delta_M, & E_{\downarrow}^1(X) &= \Delta_M, \\ E_{\uparrow}^2(X) &= \frac{1}{2} \left(\Delta_M + \mu_A - \sqrt{(\Delta_M - \mu_A)^2 + 16t^2} \right), & E_{\downarrow}^2(X) &= \frac{1}{2} \left(-\Delta_M + \mu_A - \sqrt{(\Delta_M + \mu_A)^2 + 16t^2} \right), \\ E_{\uparrow}^3(X) &= \frac{1}{2} \left(\Delta_M + \mu_A + \sqrt{(\Delta_M - \mu_A)^2 + 16t^2} \right), & E_{\downarrow}^3(X) &= \frac{1}{2} \left(-\Delta_M + \mu_A + \sqrt{(\Delta_M + \mu_A)^2 + 16t^2} \right), \end{aligned} \quad (\text{S26})$$

where we require the labelling with i such that $E_{\uparrow}^i(X) = E_{\downarrow}^i(X)$ in the non-magnetic case ($\Delta_M = 0$). Then the non-relativistic spin splitting at the $\mathbf{k} = X$ point is given by $\delta^i(X) = |E_{\uparrow}^i(X) - E_{\downarrow}^i(X)|$ (for $\Delta_M \ll 1$, when the bands stay close to the non-magnetic bands) and reads

$$\begin{aligned} \delta^1(X) &= 2\Delta_M, \\ \delta^2(X) &= \left| \Delta_M - \sqrt{(\Delta_M - \mu_A)^2 + 16t^2} + \sqrt{(\Delta_M + \mu_A)^2 + 16t^2} \right| = \Delta_M \left| 1 + \frac{\mu_A}{t} + \mathcal{O}(t^{-2}) \right|, \\ \delta^3(X) &= \left| \Delta_M + \sqrt{(\Delta_M - \mu_A)^2 + 16t^2} - \sqrt{(\Delta_M + \mu_A)^2 + 16t^2} \right| = \Delta_M \left| 1 - \frac{\mu_A}{t} + \mathcal{O}(t^{-2}) \right|. \end{aligned} \quad (\text{S27})$$

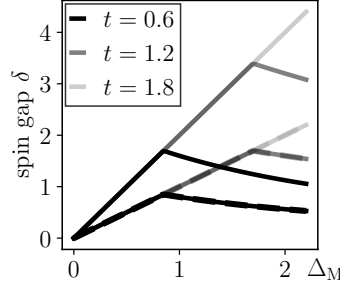


FIG. S6. Magnitude of the spin gap δ as a function of the magnetic order parameter magnitude Δ_M for several values of NN hopping t with $t' = t/2$. The kinks correspond to level crossings of the altermagnetic bands, so the linear scaling abruptly changes there.

Hence the spin gap $\delta^i(X)$ scales linearly in Δ_M for $\Delta_M \ll t$ in accordance with an AFM band gap. As depicted in Fig. S6 this linear regime extends over a broad range of order parameter sizes until a level crossing of the spin polarized bands sets in.

A non-itinerant mechanism to generate altermagnetic order usually relies on strong magnetic exchange interactions. They are hence operated in a regime where the magnetic order is much larger than the local symmetry breaking term. In this limit, corresponding to $t \ll \Delta_M$, the spin gap of our system is given with reference to the AFM state in the BC subsystem by $\bar{\delta}(X) \propto t^2/|\Delta_M - \mu_A|$. Hence, the AM spin splitting is determined by the effective hopping term that transforms non-trivially under C_4 (cf. Section S2) in accordance with the effective AM toy models discussed, e.g., in Ref. [20]. The transition between an “itinerant gap” and a “local gap” can be seen in Fig. S6, where the kink at $\Delta_M \approx 1$ corresponds to the change of reference state.

S7. REALIZATION IN AN OPTICAL LATTICE

The altermagnetic Hubbard model on the Lieb lattice consists of NN hopping t and NNN hopping t' . In this section, we discuss a possible realization of the single particle band structure of such a model in an optical lattice platform. We begin with the following lattice potential:

$$V(x, y) = -E_R[V_1(x, y) + V_2(x, y)], \quad (\text{S28})$$

$$V_1(x, y) = v_1[\cos(2\kappa x) + \cos(2\kappa y) + r(\cos(4\kappa x) + \cos(4\kappa y))]^2, \quad (\text{S29})$$

$$V_2(x, y) = 4v_2[\sin^2(\kappa(x + y)) + \sin^2(\kappa(x - y))], \quad (\text{S30})$$

where $E_R = \hbar^2 \kappa^2 / 2m$ is the recoil energy, m is the mass of ultra-cold atoms trapped into the potential wells and $\kappa = \pi/\lambda$. Figure S7a illustrates this lattice potential for $(v_1, v_2, r) = (4.0, 4.0, 0.7)$.

In Fig. S7b, we sketch the experimental setup yielding the potential of the form given by Eq. (S28). $V_1(x, y)$ can be generated by two laser sources that result in two pairs of phase-locked counter-propagating beams with wavelengths $\lambda/2$ and λ shown by thick and thin blue lines respectively in Fig. S7b. Both beams are linearly polarized with the direction of polarization aligned out of plane. Here, $r = \frac{|\vec{E}_0(\lambda/2)|}{|\vec{E}_0(\lambda)|}$ denotes the ratio of the electric field amplitudes of the two beams. On the other hand, to generate $V_2(x, y)$ one needs a linearly polarized single laser source yielding a pair of phase locked counter propagating waves of wavelength 2λ where the plane of polarization resides within the plane (shown by red lines in Fig. S7b). Notice that this beam is rotated by 45° with respect to the previous one. Such arrangement leads to a Lieb lattice with lattice periodicity λ .

Furthermore we follow standard techniques for calculation of the single particle band structure in a lattice potential. This includes numerically solving Schrödinger’s equation with potential $V(x, y)$. As a result, we obtain band structures displayed in the top panels of Fig. S7c for different parameter choices. A comparison of these spectra with the single particle band structures obtained from the model Hamiltonian (cf. Eq. (1) of the main text) for corresponding values of the tight binding parameters is given in the bottom panels of Fig. S7c. The good agreement suggests a tangible realization of the itinerant AM phase transition in optical lattice systems. In addition, there are other proposals [65, 66] suitable for the realization of an NN Lieb lattice tight-binding model.

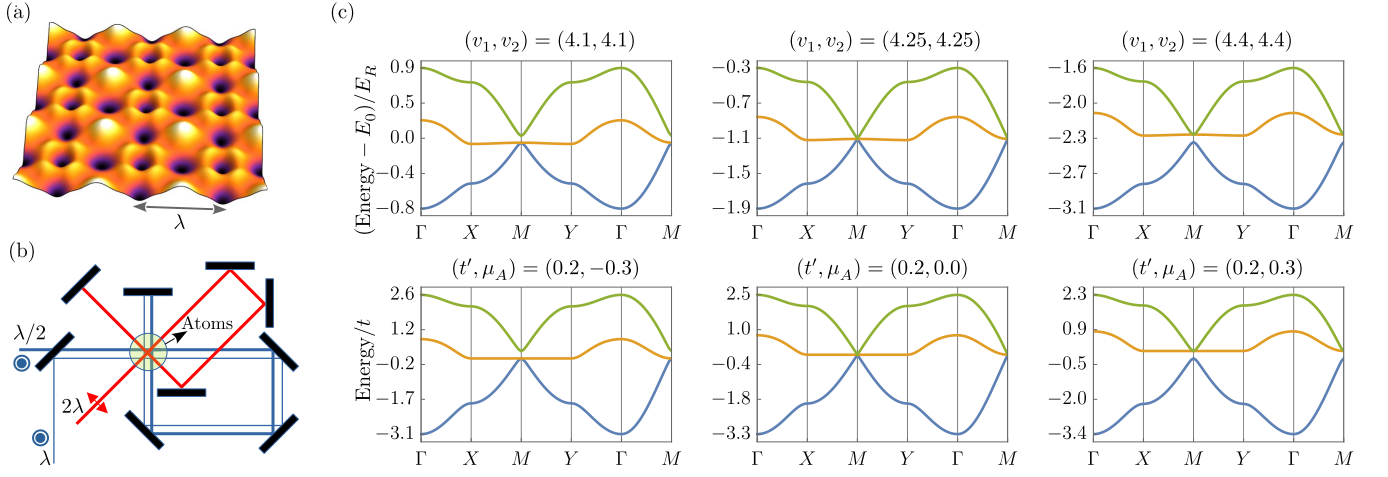


FIG. S7. Possibility of realization Lieb system in an optical lattice simulator. (a) Optical lattice potential given by Eq. (S28) with $(v_1, v_2, r) = (4.0, 4.0, 0.7)$, (b) Experimental setup. (c) top panels: optical lattice band structure (single particle) for (v_1, v_2) given by $(4.1, 4.1)$, $(4.25, 4.25)$ and $(4.1, 4.1)$ respectively and $r = 0.7$. We consider the energy offset as $E_0 = 26E_R$. (c) bottom panels: Tight binding band structure with (t', μ_A) given by $(0.2, -0.3)$, $(0.2, 0.0)$ and $(0.2, 0.3)$ in Eq. (1) where μ_A and t' are scaled with t .